



Rapid complete reconfiguration induced actual active species for industrial hydrogen evolution reaction

Received: 26 May 2022

Accepted: 23 September 2022

Published online: 02 October 2022

Check for updates

Luqi Wang¹, Yixin Hao¹, Liming Deng¹, Feng Hu¹, Sheng Zhao¹, Linlin Li¹ & Shengjie Peng¹

Rational regulation of electrochemical reconfiguration and exploration of activity origin are important foundations for realizing the optimization of electrocatalyst activity, but rather challenging. Herein, we potentially develop a rapid complete reconfiguration strategy for the heterostructures of CoC_2O_4 coated by MXene nanosheets ($\text{CoC}_2\text{O}_4@\text{MXene}$) during the hydrogen evolution reaction (HER) process. The self-assembled $\text{CoC}_2\text{O}_4@\text{MXene}$ nanotubular structure has high electronic accessibility and abundant electrolyte diffusion channels, which favor the rapid complete reconfiguration. Such rapid reconfiguration creates new actual catalytic active species of $\text{Co}(\text{OH})_2$ transformed from CoC_2O_4 , which is coupled with MXene to facilitate charge transfer and decrease the free energy of the Volmer step toward fast HER kinetics. The reconfigured components require low overpotentials of 28 and 216 mV at 10 and 1000 mA cm^{-2} in alkaline conditions and decent activity and stability in natural seawater. This work gives new insights for understanding the actual active species formation during HER and opens up a new way toward high-performance electrocatalysts.

Hydrogen fuel with high mass specific energy density and environmental friendliness is an excellent energy carrier, contributing to the realization of carbon neutrality^{1–3}. Electrocatalytic water splitting is an economical and efficient method for hydrogen production^{4,5}. The hydrogen evolution reaction (HER) as one of the half-reactions of water splitting is an important factor affecting hydrogen production technology, which requires the development of efficient HER catalysts with fast kinetics^{6–9}. In this regard, the benchmark Pt catalyst is still considered to be the most efficient commercial electrocatalyst for HER. However, they usually suffer from scarcity, high cost, and long-term instability^{10–12}. Thus far, transition metal-based materials have turned to be the promising alternatives to noble metal catalysts because of their lower cost and appropriate electronic structure^{13,14}. It is reported that they are prone to involving surface reconfiguration processes through electrochemical activation under complex conditions of catalytic reactions, ultimately exhibiting excellent catalytic

performance^{15–17}. Therefore, it is greatly attractive if this electrochemical reconfiguration can be utilized to develop new electrocatalysts. However, reconfigured catalysts usually present multiple components and valence states, which complicate the dynamic evolution process, resulting in extremely impediment to the identification of actual catalytic active species and the understanding of catalytic origins^{18,19}. As a result, exploring the dynamic reconfiguration mechanism of catalysts and revealing the actual catalytic active species are beneficial to the accurate design of high-efficiency nonprecious metal-based electrocatalysts.

Typically, oxygen evolution reaction (OER) catalysts would undergo a surface reconfiguration process to form highly active metal oxides or (oxy)hydroxides species under electro-oxidative conditions, which have been confirmed as the actual active phase^{20,21}. However, the catalytic surface reconfiguration process to improve the electrocatalytic activity rarely occurs during HER^{22,23}. Normally, the HER

¹Jiangsu Key Laboratory of Electrochemical Energy Storage Technologies, College of Materials Science and Technology, Nanjing University of Aeronautics and Astronautics, Nanjing 210016, China. ✉ e-mail: pengshengjie@nuaa.edu.cn

catalysts generally exhibit a near-surface nanoscale reconfiguration, such as a core-shell structure, containing numerous internal inert components²⁴. Due to their restrictive surface-active area, the derived catalysts reveal incompletely exploited catalytic activity, resulting in low component utilization^{25,26}. Meanwhile, the complex composition of the surface-reconfigured catalysts has greatly hindered the in-depth exploration of catalytic origins^{27,28}. Considering these aspects, the rational design of catalysts with special structural and chemical properties to trigger complete reconfiguration can effectively eliminate the above problems. The advantages of the complete reconfiguration lie in the adequate electrolyte contact and loose reconfiguration layer for favoring the solution penetration and mass transport^{29–31}. Generally, the addition of a hydrophilic material to the catalyst to improve the wettability between the electrode and the electrolyte can assist in inducing complete reconfiguration of the catalyst²⁰. Current studies found that the introduction of MXene improved the wettability of catalyst surface, which could fully react with the electrolyte and achieve preliminary reconfiguration^{32–34}. Hence, the rational design of MXene-based catalysts is expected to achieve deep or even complete reconfiguration. Moreover, the loose reconfigured structure facilitates accelerative electrolyte supply and fast gas diffusion during vigorous electrocatalytic reactions, which is in favor of hydrogen production at high current densities^{35–37}. Meanwhile, since entire unstable components could be converted into thermodynamically steady species during the complete reconfiguration process, it can also realize outstanding catalysis durability even under terrible conditions of natural seawater^{38,39}. Therefore, engineering on the complete reconfiguration and the comprehensive understandings are believed to direct purposeful design of high-performance catalysts for industrialization promotion.

Herein, we report a significant conceptual advance of reconfiguration during the HER process based on the $\text{CoC}_2\text{O}_4@\text{MXene}$ model catalyst. The obtained heterostructured catalyst features a nanotubular structure, composed of CoC_2O_4 nanorods self-assembled with MXene due to the interface-induced effect. This favorable hydrophilic nanotubular structure can immensely increase the penetration of the electrolyte and the ultra-thin MXene with high conductivity provides an effective electronic path, which both facilitates the rapid and deep self-reconfiguration process. In addition, the loose structure is the main factor to drive complete reconfiguration. In-situ characterization techniques and X-ray absorption spectroscopy demonstrate the actual active species of $\text{Co}(\text{OH})_2$ transformed from CoC_2O_4 . The reconfigured components can manipulate the electron delocalization and reduce the energy barrier, leading to fast electron transfer. More importantly, such rapid reconfiguration introduces a highly disordered structure of $\text{Co}(\text{OH})_2$ with abundant exposed Co active sites, which can facilitate the adsorption of water molecules and optimize the binding energies of H^* intermediates, and thus eventually contributes to the HER kinetics. As a result, the synergistic interaction between $\text{Co}(\text{OH})_2$ and MXene ensures remarkable HER activity even at a high current density. Specifically, the reconfigured $\text{CoC}_2\text{O}_4@\text{MXene}$ delivers small overpotentials of 28 and 216 mV to reach current densities of 10 and 1000 mA cm^{-2} in 1 M KOH, respectively. Even in alkaline and neutral seawater, the reconfigured $\text{CoC}_2\text{O}_4@\text{MXene}$ exhibits superior and stable HER performance. This study not only provides idealized electrocatalysts for highly efficient HER under various conditions but also unprecedentedly reveals the rapid complete reconfiguration during the HER, thereby giving a deep understanding for the performance-enhanced origin and insights into future catalyst design.

Results

Synthesis and characterization of morphologies and structures

An interface-induced self-assembly strategy is employed to synthesize the hollow nanotube $\text{CoC}_2\text{O}_4@\text{MXene}$ pre-catalyst, which is specifically described in Fig. 1a. Briefly, MXene nanosheets were obtained by

selective etching of Al element in MAX phase (Ti_3AlC_2) by LiF/HCl acid and the following subsequent exfoliation (Supplementary Fig. 1). After etching and ultrasonic exfoliation treatments, the XRD characteristic peak of Ti_3AlC_2 disappears and exhibits a typical peak at 6.1° corresponding to the (002) peak (Supplementary Figs. 2 and 3), demonstrating that Ti_3AlC_2 has completely converted to $\text{Ti}_3\text{C}_2\text{T}_x$ MXene⁴⁰. Subsequently, the $\text{CoC}_2\text{O}_4@\text{MXene}$ hybrid is finally obtained through dropping oxalic acid dihydrate ($\text{H}_2\text{C}_2\text{O}_4 \cdot 2\text{H}_2\text{O}$) aqueous solution into the mixture of $\text{Co}(\text{NO}_3)_2 \cdot 2\text{H}_2\text{O}$ aqueous solution and MXene nanosheets with continuous stirring under room-temperature. Specifically, CoC_2O_4 crystal nuclei are formed on the surface of MXene and grow along a crystal orientation to form nanorod aggregates⁴¹. And then the aggregates are crosslinked as well as self-assembled into tubular structures, which might be attributed to the inductive effect between MXene and CoC_2O_4 to achieve low surface energy.

The scanning electron microscopy (SEM) images reveal that $\text{CoC}_2\text{O}_4@\text{MXene}$ exhibits nanotube morphology in Fig. 1b, c. Notably, a rough surface is presented on $\text{CoC}_2\text{O}_4@\text{MXene}$ compared with the pristine CoC_2O_4 nanorods (Supplementary Fig. 4). The special morphology is attributed to the MXene coating during the self-assembly of cobalt oxalate, while the ultrathin structure and surface functional groups of MXene nanosheets provide more flexibility for curling (Supplementary Figs. 5 and 6). Because of the opposite surface charges, the electrostatic adsorption force between MXene and CoC_2O_4 induces curling of MXene (Supplementary Fig. 7). As the crystal continues to grow, CoC_2O_4 evolves into a nanotube-like structure accompanied by an adhesive MXene layer (Fig. 1d, e), which is further demonstrated by the open-end hollow nanorods with a well-defined outline and certain curvature in Supplementary Fig. 8. The corresponding high-resolution transmission electron microscope (HRTEM) image presents the typical boundary area of CoC_2O_4 and MXene with clearly different diffractive contrast in Fig. 1f, indicating that MXene is successfully coated on the surface of CoC_2O_4 . Consistently, the lattice fringe with an interplanar spacing of 0.306 nm is indexed to the (114) plane of CoC_2O_4 (Fig. 1g), while a d-spacing of around 0.95 nm corresponds to the typical interlayer of MXene. Furthermore, the fast Fourier transformation image reveals the existence of the crystal phase of $\text{CoC}_2\text{O}_4@\text{MXene}$, which is consistent with the XRD results (Fig. 1h). Meanwhile, the uniform distribution mapping images of Co, Ti, O, and C elements also demonstrate the successful synthesis of MXene coated CoC_2O_4 (Fig. 1i). The tubular hybrid not only presents a higher specific surface area (Supplementary Fig. 9) but also exhibits abundant diffusion channels to activate the diffusion dimension of the electrolyte and unfreeze the restriction of mass transport. Even the electrolyte could enter the interior of the $\text{CoC}_2\text{O}_4@\text{MXene}$ matrix, providing a larger electrolyte-electrocatalyst interface. Moreover, the introduction of highly hydrophilic MXene significantly improves water adsorption and electrode wettability, as shown by contact angle (CA) measurements (Supplementary Fig. 10). This unique structure provides the feasibility for spontaneous rapid complete reconfiguration.

Electrochemical active site modulation

To correlate the rapid reconfiguration of $\text{CoC}_2\text{O}_4@\text{MXene}$ with the improvement of catalytic activity during HER, the continuous LSV curves (5 mV s^{-1} scan rate) were tested in 1 M KOH. The overpotential of $\text{CoC}_2\text{O}_4@\text{MXene}$ decreased drastically with increasing LSV scan number to achieve a stable polarization curve after 5 cycles, indicating the possibility of reconfiguration of $\text{CoC}_2\text{O}_4@\text{MXene}$ during HER (Fig. 2a). The corresponding overpotentials (@10 mA cm^{-2}) are plotted as a function of the LSV scan number in Fig. 2b. When the initial $\text{CoC}_2\text{O}_4@\text{MXene}$ was subjected to continuous LSV scans for only 5 cycles, the overpotential strikingly decreases by approximately 46 mV, resulting in a low overpotential of 28 mV at 10 mA cm^{-2} . Moreover, chronopotentiometry measurement also further verified the reconfiguration phenomenon of $\text{CoC}_2\text{O}_4@\text{MXene}$ (Supplementary Fig. 11).

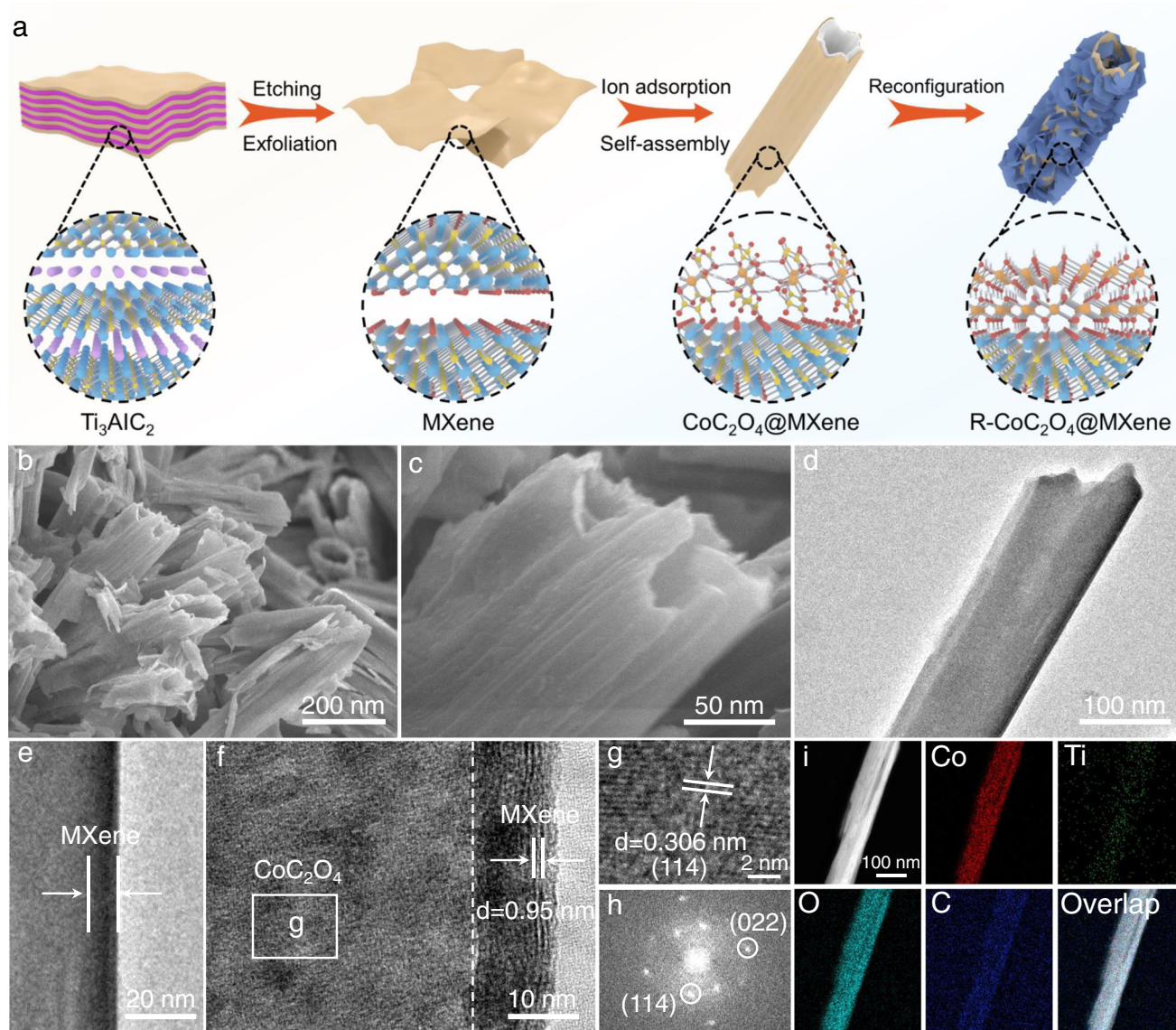


Fig. 1 | Structural characterization of the fabricated CoC_2O_4 @MXene pre-catalyst. **a** Schematic illustration for the synthesis process of CoC_2O_4 @MXene. **b, c** SEM, **(d, e)** TEM, **(f, g)** HRTEM images of CoC_2O_4 @MXene. **h** Fast Fourier

transformation (FFT) image. **i** Elemental mapping revealing the presence and homogenous distribution of Co, Ti, O, and C elements in CoC_2O_4 @MXene.

CoC_2O_4 @MXene exhibits the advantages of rapid reconfiguration and superior performance compared to recently reported HER pre-catalysts (Supplementary Table 1). The CoC_2O_4 without MXene coating also implies similar reconfiguration behavior, whereas the reconfiguration speed is tardy and the performance increase is much worse than CoC_2O_4 @MXene (Supplementary Fig. 12). MXene can effectively enhance adsorbate accumulation and charge transfer through the analysis of mass transfer kinetics on the catalytic surface, which significantly facilitates the reconfiguration process (Supplementary Fig. 13). CoC_2O_4 @MXene and CoC_2O_4 after electrochemical reconfiguration (repeated LSV scans) are denoted as R- CoC_2O_4 @MXene and R- CoC_2O_4 . These results demonstrate that the CoC_2O_4 @MXene tubular catalyst with good hydrophilicity can increase the penetration of the electrolyte compared to the rod-shaped CoC_2O_4 , benefiting the rapid reconfiguration.

The physical structure variations of the R- CoC_2O_4 @MXene catalyst are firstly investigated to further explore the actual active species of HER after reconfiguration. Only peaks corresponding to $\text{Co}(\text{OH})_2$ can be observed in the XRD patterns of R- CoC_2O_4 @MXene, whereas

R- CoC_2O_4 manifests an incompletely reconfigured multi-component composite structure (Supplementary Fig. 14). The morphological difference in catalysts before and after electrochemical treatment can be traced back to this transformation. R- CoC_2O_4 @MXene exhibits a large number of hexagonal nanosheets interconnected to form a hollow rod-like loose structure (Supplementary Fig. 15), which allows deep penetration of alkaline electrolyte to stimulate catalytic reactions and complete reconfiguration. The TEM image of R- CoC_2O_4 @MXene also shows the reconfigured loose nanorod structure and the ultrathin MXene nanosheets ideally adhere to nanorods (Supplementary Fig. 16). The HRTEM image reveals that these hexagonal nanosheets can be attributed to the formation of $\text{Co}(\text{OH})_2$, in which the lattice fringes are 0.276 nm to comply with the (100) plane of $\text{Co}(\text{OH})_2$ (Fig. 2c). In essence, the loose derivatization layer promotes the deep penetration of electrolyte, triggering a chain of evolutions till complete reconfiguration. However, the rod-like structure of pristine CoC_2O_4 is difficult to be completely hydrolyzed by the electrolyte, since the formed tight layer hinders the solution penetration for further reconfiguration (Supplementary Fig. 17). To reveal the special

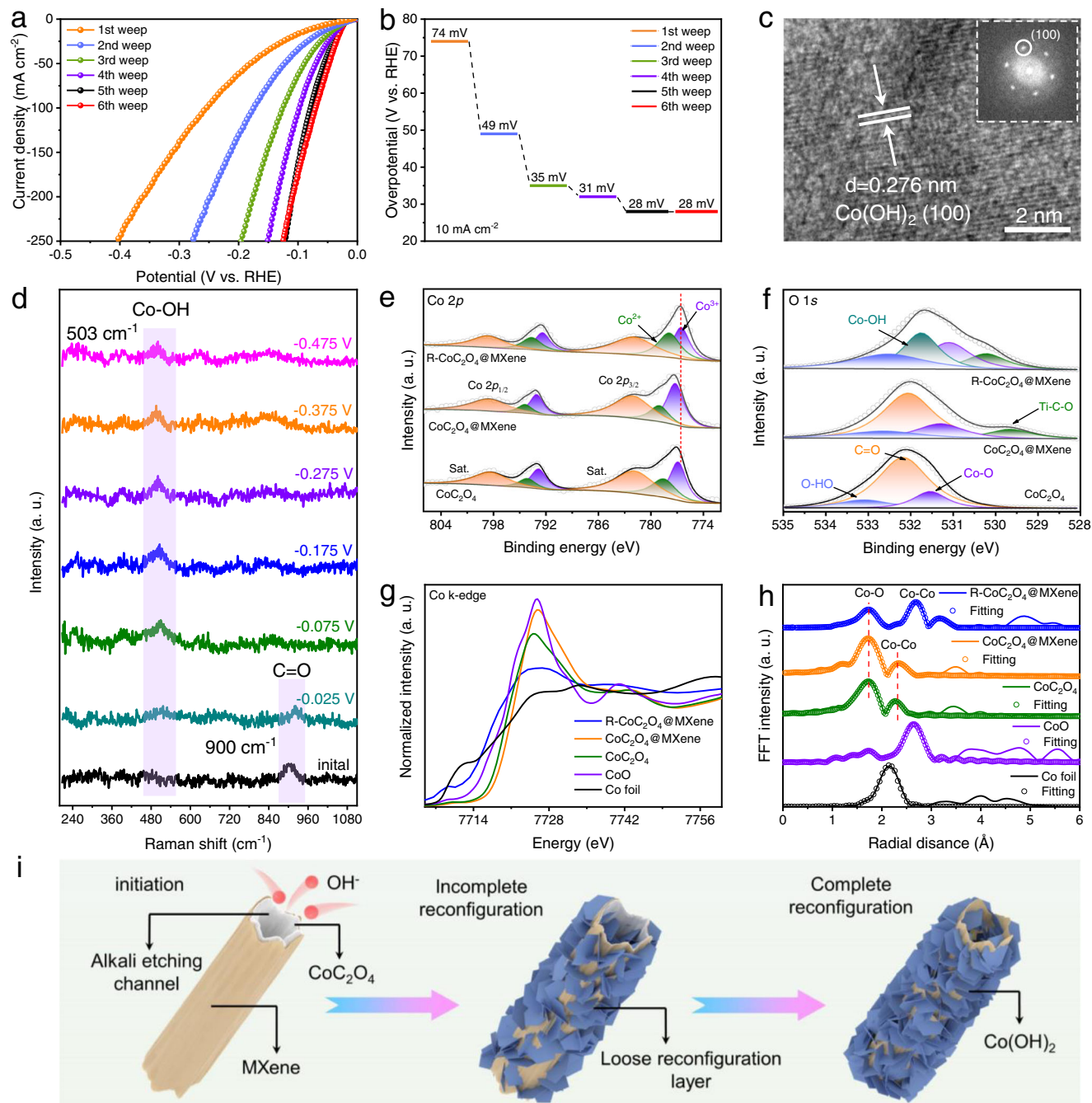


Fig. 2 | Mechanism analysis of reconfiguration processes during HER.

a Polarization curves of different LSV scans (IR correction) and **(b)** corresponding overpotentials of $\text{CoC}_2\text{O}_4@\text{MXene}$ in 1 M KOH solution. **c** HRTEM image of $\text{R-CoC}_2\text{O}_4@\text{MXene}$. **d** In-situ Raman spectra of $\text{CoC}_2\text{O}_4@\text{MXene}$. XPS spectra of the

(e) $\text{Co } 2p$ and **(f)** $\text{O } 1s$ regions for $\text{R-CoC}_2\text{O}_4@\text{MXene}$, $\text{CoC}_2\text{O}_4@\text{MXene}$, and CoC_2O_4 respectively. **g** Co K-edge XANES spectra and **(h)** FT-EXAFS spectra of the $\text{R-CoC}_2\text{O}_4@\text{MXene}$, $\text{CoC}_2\text{O}_4@\text{MXene}$, CoC_2O_4 , CoO , and Co foil. **i** Reconfiguration process schematic diagram from $\text{CoC}_2\text{O}_4@\text{MXene}$ to $\text{R-CoC}_2\text{O}_4@\text{MXene}$.

properties of reconfigured $\text{R-CoC}_2\text{O}_4@\text{MXene}$, $\text{Co(OH)}_2@\text{MXene}$ is prepared by a classical method for comparison (Supplementary Figs. 18 and 19). The Co(OH)_2 in $\text{R-CoC}_2\text{O}_4@\text{MXene}$ and the as-prepared $\text{Co(OH)}_2@\text{MXene}$ have consistent crystal structures analyzed by SAED and HRTEM (Supplementary Fig. 20). Interestingly, the HRTEM of $\text{R-CoC}_2\text{O}_4@\text{MXene}$ exhibits partial lattice ambiguity regions compared to $\text{Co(OH)}_2@\text{MXene}$, which implies the generation of defect structures. Moreover, $\text{R-CoC}_2\text{O}_4@\text{MXene}$ inherits the excellent wettability of $\text{CoC}_2\text{O}_4@\text{MXene}$ and outperforms the as-prepared $\text{Co(OH)}_2@\text{MXene}$. In-situ Raman spectra were applied to detect the reconfiguration process of the catalyst in real-time. Firstly, the local

structure of the initial $\text{CoC}_2\text{O}_4@\text{MXene}$ is detected without applied potential and electrolyte, in which the detectable bands centered at 900 cm^{-1} belong to the C=O vibration in CoC_2O_4 (Fig. 2d and Supplementary Fig. 21). Subsequently, the C=O vibration completely disappears when the potential was applied in 1 M KOH solution, while new broadband of 503 cm^{-1} appears due to the Co-OH vibration in Co(OH)_2 ^{24,25}. This is also consistent with the Co-OH characteristic peak positions in the as-prepared $\text{Co(OH)}_2@\text{MXene}$ (Supplementary Fig. 22). This fact suggests that the application of potential in alkaline solution can trigger the rapid destruction of the C=O bond. Meanwhile, a large number of hydroxide ions in the electrolyte are immediately

supplied to form Co–OH coordination, which reveals the transformation mechanism of CoC_2O_4 to $\text{Co}(\text{OH})_2$. In this regard, the reconfiguration process of the pre-catalyst CoC_2O_4 @MXene is illustrated in Fig. 2i. XRD of CoC_2O_4 @MXene immersed in 1 M KOH and performed neutral HER confirm the importance of the applied potential and alkali etching to drive the reconfiguration (Supplementary Fig. 23). The morphological difference between $\text{R-CoC}_2\text{O}_4$ @MXene and CoC_2O_4 @MXene soaked in 1 M KOH for 24 h intuitively indicates the driving of the reconfiguration by the applied potential (Supplementary Fig. 24).

The surface chemical states and electronic interaction during the reconfiguration process are examined by X-ray photoelectron spectroscopy (XPS) (Supplementary Fig. 25). The Co 2*p* spectrum of CoC_2O_4 @MXene is significantly shifted to higher binding energy (Fig. 2e), indicating that the valence state of the Co species is elevated. The higher valence Co atoms in CoC_2O_4 @MXene favor electron acquisition, which provides a prerequisite for the reconfiguration of the catalyst. The Co 2*p* of the reconfigured $\text{R-CoC}_2\text{O}_4$ @MXene is shifted towards lower binding energy, indicating that the reconfiguration can further optimize the electronic structure of the catalyst. Moreover, the binding energy of the Co 2*p* spectrum of $\text{R-CoC}_2\text{O}_4$ @MXene is lower than that of $\text{Co}(\text{OH})_2$ @MXene due to the reduction potential of HER (Supplementary Fig. 26). Meanwhile, the Co 2*p* spectrum of $\text{R-CoC}_2\text{O}_4$ @MXene is negatively shifted compared with CoC_2O_4 @MXene soaked in 1 M KOH for 24 h, which further verified the formation of low-valent Co species under HER potential conditions (Supplementary Fig. 27). Remarkably, the exfoliated MXene possesses a large number of C–Ti–O polar bonds, which facilitates the directional charge transfer between the host material and the carrier (Fig. 2f)⁴². Moreover, the introduction of MXene can alleviate the limitation of electron transmission and a continuous supply of electrons for the deep reconfiguration of CoC_2O_4 . The appearance of Co–OH bonds in the O 1*s* XPS spectra of $\text{R-CoC}_2\text{O}_4$ @MXene also confirms the formation of $\text{Co}(\text{OH})_2$.

X-ray absorption fine structure (XAFS) analysis is beneficial for the further investigation of the electronic structure and coordination environment of elements. The X-ray absorption near edge structure (XANES) of Co K-edge spectra of CoC_2O_4 @MXene has a slight shift to higher energies compared to CoC_2O_4 (Fig. 2g), indicating the decreased electron density at the Co sites. When Co^{2+} is oxidized to a high valence state, a charge transport orbit can be acquired for efficient electron transfer at the electrode-electrolyte interface, which provides a steady stream of electrons for catalyst reconfiguration. Additionally, the absorption edge of the $\text{R-CoC}_2\text{O}_4$ @MXene shifts to lower energy relative to that of the CoC_2O_4 @MXene, implying that the catalyst reconfiguration promotes charge redistribution, resulting in faster charge transfer in electrochemical reactions and enhanced catalytic activity. A similar oscillation with significant intensity reduction is observed for $\text{R-CoC}_2\text{O}_4$ @MXene, indicating that the reconfiguration induces a different coordination environment (Supplementary Fig. 28). From extended XAFS (EXAFS) of Co K-edge (Fig. 2h), the dominant peak is assigned to the single scattering paths of the nearest Co–O shell, followed by one specific Co–Co shell. The fitting result of $\text{R-CoC}_2\text{O}_4$ @MXene shows that the Co–Co distance in the first shell is 3.097 Å larger than that of CoC_2O_4 (2.652 Å) and CoC_2O_4 @MXene (2.658 Å) (Supplementary Table 2), indicating the $\text{R-CoC}_2\text{O}_4$ @MXene catalyst undergoes the reconfiguration⁴³. The coordination number of Co–O decreases from 5.9 (CoC_2O_4 @MXene) to 5.5 ($\text{R-CoC}_2\text{O}_4$ @MXene), efficiently demonstrating the presence of coordinatively unsaturated Co sites⁴⁴. These results are also confirmed in the wavelet transform (WT) (Supplementary Fig. 29). As shown in Supplementary Fig. 30, the adsorption edge of $\text{R-CoC}_2\text{O}_4$ @MXene is shifted to lower energy compared to $\text{Co}(\text{OH})_2$ @MXene and $\text{Co}(\text{OH})_2$, indicating the formation of low-valence Co species. The similar peak positions of Co–Co and Co–O bonds demonstrate the existence of $\text{Co}(\text{OH})_2$ in

$\text{R-CoC}_2\text{O}_4$ @MXene. More importantly, the electron paramagnetic resonance (EPR) detection found that $\text{R-CoC}_2\text{O}_4$ @MXene possesses more oxygen defects than the $\text{Co}(\text{OH})_2$ @MXene prepared by the classical method (Supplementary Fig. 31), which provides the activity for the H adsorption site. This is also verified by the weaker Co–O bond in CoC_2O_4 @MXene compared to $\text{Co}(\text{OH})_2$ @MXene in Co K-edge EXAFS spectra. The XPS and XANES analysis synergistically verify that $\text{R-CoC}_2\text{O}_4$ @MXene induced by electron availability exhibits optimized electronic structure and exposed metal active sites, which lays the foundation for optimizing the intrinsic activity and increasing catalytic active sites.

HER activity of reconfigured components

The electrocatalytic HER performance of various catalysts was examined in 1.0 M KOH to display the advantage of the in-situ reconfigured $\text{R-CoC}_2\text{O}_4$ @MXene. The HER performance of $\text{R-CoC}_2\text{O}_4$ @MXene synthesized with 20 mL MXene solution is the best among the counterparts with different ratios of CoC_2O_4 and MXene (Supplementary Fig. 32). The optimized $\text{R-CoC}_2\text{O}_4$ @MXene requires a lower overpotential of 28 mV to achieve a current density of 10 mA cm^{−2} compared to $\text{R-CoC}_2\text{O}_4$ (148 mV) and MXene (169 mV) (Fig. 3a). In particular, the current density of $\text{R-CoC}_2\text{O}_4$ @MXene catalyst can reach 500 and 1000 mA cm^{−2} at overpotentials of 157 and 216 mV, which are much higher than that of commercial Pt/C, and its highest current density can reach up to 1300 mA cm^{−2} for potential industrial application. The corresponding Tafel slope of $\text{R-CoC}_2\text{O}_4$ @MXene (43 mV dec^{−1}) is close to Pt/C (38 mV dec^{−1}), indicating strong HER kinetics (Fig. 3b)⁴⁵. Electrochemical impedance spectroscopy (EIS) shows that $\text{R-CoC}_2\text{O}_4$ @MXene has lower charge transfer resistance (Supplementary Fig. 33 and Table 3), which is attributed to the efficient electron transfer channel between MXene and low-valence $\text{Co}(\text{OH})_2$. The high exchange current density also verifies the optimized electron transport (Supplementary Fig. 34). In addition, $\text{R-CoC}_2\text{O}_4$ @MXene exhibits higher mass activity than commercial Pt/C (Supplementary Fig. 35). The higher turnover frequency (TOF) of $\text{R-CoC}_2\text{O}_4$ @MXene verifies the excellent intrinsic activity (Fig. 3c). The electrochemical surface area (ECSA) value of $\text{R-CoC}_2\text{O}_4$ @MXene is about 5.36 times higher than that of $\text{R-CoC}_2\text{O}_4$, revealing more HER active sites (Supplementary Fig. 36 and Table 4).

To understand the performance difference between $\text{R-CoC}_2\text{O}_4$ @MXene and Pt/C catalysts, the release manner of the H₂ bubbles during HER was investigated to evaluate the mass transfer ability. The diameters of H₂ bubbles are small on $\text{R-CoC}_2\text{O}_4$ @MXene (Fig. 3d), while they become larger with increasing current density on the Pt/C electrode. For $\text{R-CoC}_2\text{O}_4$ @MXene, the majority of the detached bubbles were within the size of 0.2–0.3 mm at the current density of 1000 mA cm^{−2}, which is much smaller than the bubble diameter of the Pt/C electrode (Fig. 3e). These results indicate the superior mass transfer ability of $\text{R-CoC}_2\text{O}_4$ @MXene at high current densities. The relationship between current density and $\Delta\eta/\Delta\log |j|$ was analyzed to evaluate the high current density HER performance of $\text{R-CoC}_2\text{O}_4$ @MXene (Fig. 3f)^{35,46}. When the current density increases to 500 mA cm^{−2}, the ratio for $\text{R-CoC}_2\text{O}_4$ @MXene (145 mV dec^{−1}) is much smaller than that Pt/C (220 mV dec^{−1}), but is still less than 174 mV dec^{−1} for $\text{R-CoC}_2\text{O}_4$ @MXene at a current density of 1000 mA cm^{−2}, indicating brilliant catalytic performance for high current density HER. A chronoamperometry test in Fig. 3g demonstrates that $\text{R-CoC}_2\text{O}_4$ @MXene could maintain stability with little decay at current densities of 10, 500, and 1000 mA cm^{−2} up to 100 h. The excellent durability is further confirmed by CV after 3000 cycles (Supplementary Fig. 37). After the durability test, $\text{R-CoC}_2\text{O}_4$ @MXene still maintains its original phase, demonstrating the robust structure of $\text{R-CoC}_2\text{O}_4$ @MXene (Supplementary Fig. 38). It is summarized that the HER performance of the $\text{R-CoC}_2\text{O}_4$ @MXene is superior to most reported electrocatalysts in terms of both the low current density of 10 and high current densities

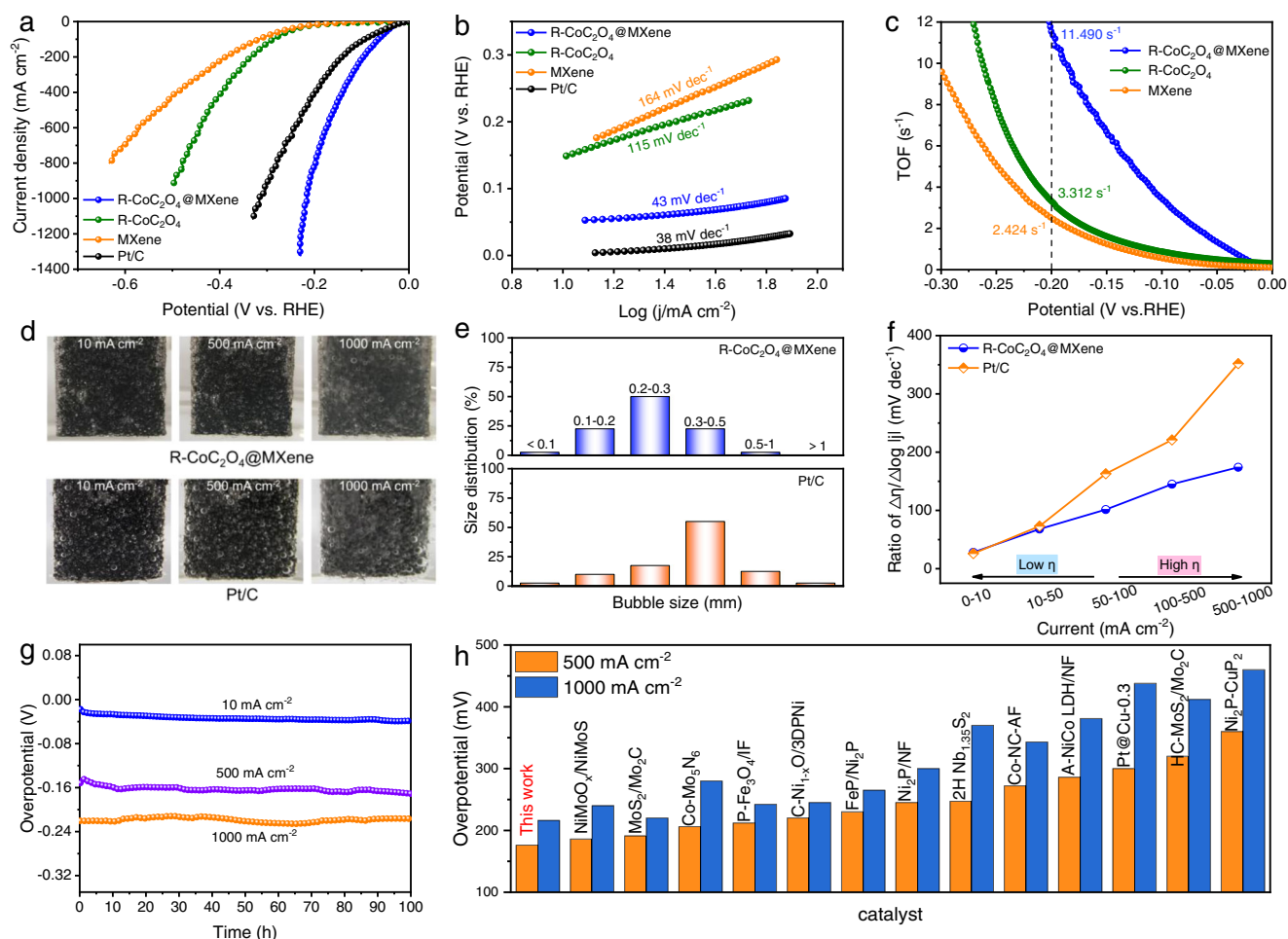


Fig. 3 | Electrochemical HER performance measurements. **a** The HER polarization curves and **(b)** Tafel slopes of MXene, R-CoC₂O₄, R-CoC₂O₄@MXene, and Pt/C. **c** The relationship between TOF and the tested potentials for MXene, R-CoC₂O₄, and R-CoC₂O₄@MXene. **d** Digital photos of H₂ bubbles during the HER process and **(e)** bubble size distributions on R-CoC₂O₄@MXene and Pt/C. **f** The ratios of $\Delta\eta/\Delta\log$

$|j|$ for Pt/C and R-CoC₂O₄@MXene at different current densities.

g Chronopotentiometry curves of R-CoC₂O₄@MXene at constant current densities of 10, 500, and 1000 mA cm⁻². **h** Comparison of overpotential (500 and 1000 mA cm⁻²) of R-CoC₂O₄@MXene with recently reported high current density HER catalysts in 1 M KOH solution.

of 500 and 1000 mA cm⁻² (Fig. 3h and Supplementary Table 5). In addition, the catalytic activity and stability of R-CoC₂O₄@MXene are obviously superior to as-prepared Co(OH)₂@MXene in 1 M KOH (Supplementary Fig. 39). As a result, the reconfigured components deliver outstanding intrinsic activity and stability for HER.

Theoretical calculation

To elucidate the relationship between the electronic structure of R-CoC₂O₄@MXene and the excellent HER catalytic activity, density functional theory (DFT) calculations were performed on the model structure (Supplementary Fig. 40). R-CoC₂O₄@MXene exhibits superior formation energies and relatively low antibonding states, verifying the stability of the computational model (Supplementary Figs. 41 and 42). The total density of states (DOS) displays that R-CoC₂O₄@MXene has a higher electron density near the Fermi level than CoC₂O₄@MXene and CoC₂O₄ (Fig. 4a and Supplementary Fig. 43). This result suggests that the complete reconfiguration of the catalyst enhances the electrical conductivity, which ensures fast electron transfer during electrocatalysis. Meanwhile, the d-band center shifts downward relative to the Fermi level from -0.514 eV in CoC₂O₄@MXene to -1.474 eV in R-CoC₂O₄@MXene (Fig. 4b)⁴⁷. The d-band center downshift weakens the binding strength with H* and facilitates the desorption of H*, which optimizes the HER reaction process. From Fig. 4c, the differential charge density of

R-CoC₂O₄@MXene exhibits significant charge accumulation around the Co atom as well as dispersion of electron states around the O atom compared to CoC₂O₄ and CoC₂O₄@MXene (Supplementary Fig. 44). This electron redistribution behavior can optimize the reaction intermediates absorption energy, thus enhancing the catalytic activity⁴⁸.

The origins for HER catalytic activity improvement were further investigated using the intermediate free energy on the CoC₂O₄, CoC₂O₄@MXene, and R-CoC₂O₄@MXene systems. As shown in Fig. 4d, R-CoC₂O₄@MXene shows more negative adsorption energy of water molecule ($\Delta E_{\text{H}_2\text{O}}$) (-1.02 eV) compared to CoC₂O₄@MXene (-0.75 eV) and CoC₂O₄ (-0.41 eV) (Supplementary Fig. 45). This suggests that the exposed Co sites are beneficial to the adsorption and activation of H₂O. Subsequently, the activated H₂O molecules undergo dissociation, in which H and OH are adsorbed to the two adjacent unsaturated Co sites, respectively (Supplementary Fig. 46). The activation energy barrier for the R-CoC₂O₄@MXene system declines to 0.51 eV during the H₂O dissociation process, as lower than that of CoC₂O₄@MXene (0.76 eV) and CoC₂O₄ (1.04 eV) (Fig. 4e)⁴⁹. The depressed Volmer step can be dramatically accelerated due to the positive effects on the thermodynamics of water adsorption and dissociation. Furthermore, the free energy of hydrogen adsorption (ΔG_{H^*}) is also an important factor to explain the HER activity, and the close to zero ΔG_{H^*} value implies reasonable H adsorption and H₂ desorption. The ΔG_{H^*} of R-CoC₂O₄@MXene is calculated to be 0.12 eV, which is

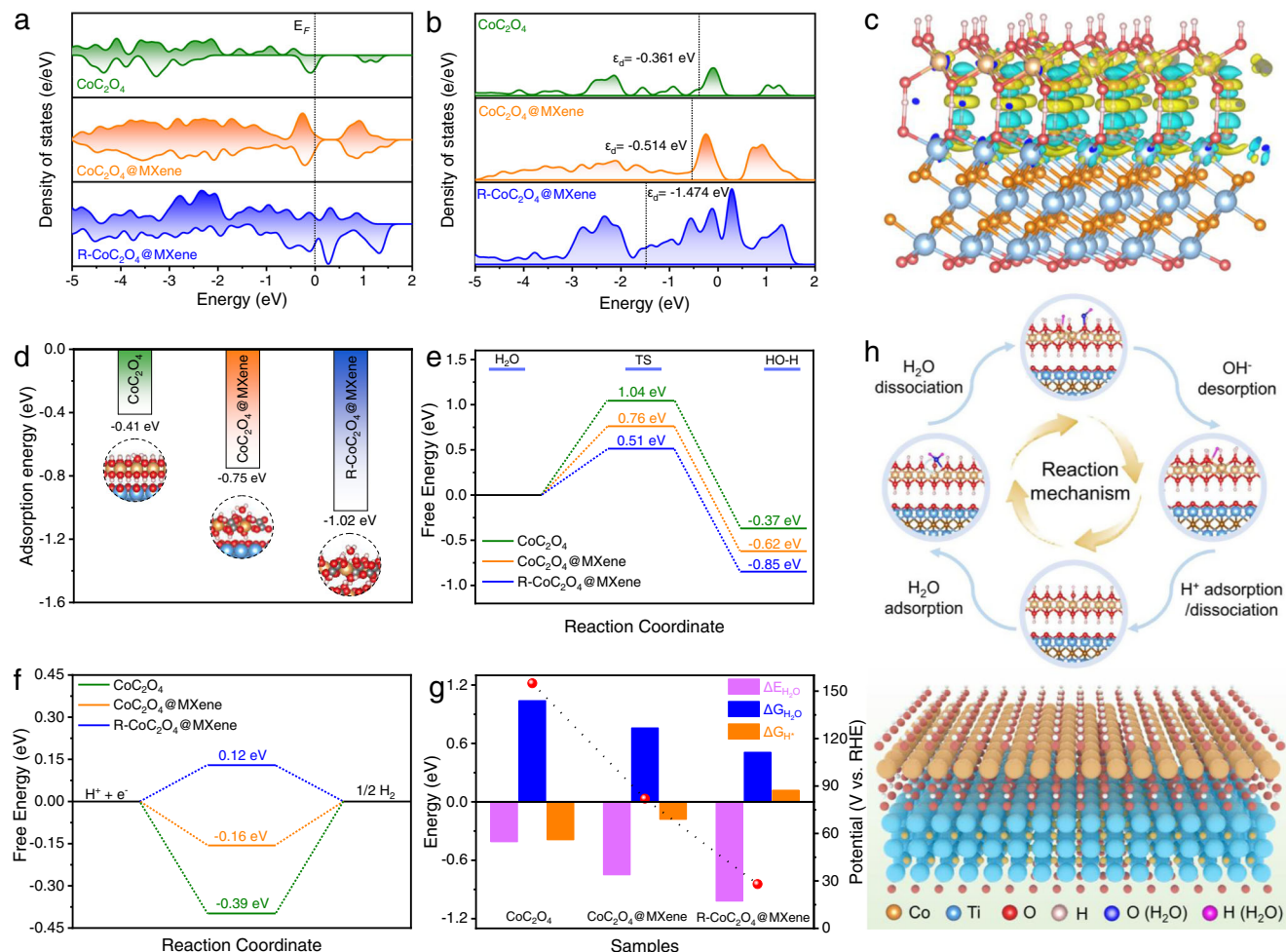


Fig. 4 | Theoretical calculation of HER activation energy. **a** The DOS plots and **(b)** D-band centers for CoC_2O_4 , $\text{CoC}_2\text{O}_4@\text{MXene}$, and $\text{R-CoC}_2\text{O}_4@\text{MXene}$. **c** Differential charge density of $\text{R-CoC}_2\text{O}_4@\text{MXene}$, the yellow and blue zones represent the charge accumulation or dispersion, respectively. **d** H_2O adsorption energy ($\Delta E_{\text{H}_2\text{O}}$), **(e)** H_2O dissociation energy ($\Delta G_{\text{H}_2\text{O}}$), and **(f)** free energy of

adsorbed H^+ intermediates (ΔG_{H^+}) on the CoC_2O_4 , $\text{CoC}_2\text{O}_4@\text{MXene}$, and $\text{R-CoC}_2\text{O}_4@\text{MXene}$, respectively. **g** The relationship between the calculated $\Delta E_{\text{H}_2\text{O}}$, $\Delta G_{\text{H}_2\text{O}}$, ΔG_{H^+} values, and the overpotential at 10 mA cm^{-2} . **h** Schematic illustration of the catalytic mechanism for alkaline HER on the $\text{R-CoC}_2\text{O}_4@\text{MXene}$.

closer to the thermoneutral value than that of the pristine CoC_2O_4 (-0.39 eV) and $\text{CoC}_2\text{O}_4@\text{MXene}$ (-0.16 eV) (Fig. 4f). This indicates a suitable reaction energy barrier for H adsorption and H_2 desorption on unsaturated Co sites (Supplementary Fig. 47). Thus, the energy barrier parameters of different reaction stages in the HER process together determine the catalytic activity, leading to a reduction in the HER overpotential (Fig. 4g). Herein, the HER mechanism of exposed Co active sites in $\text{R-CoC}_2\text{O}_4@\text{MXene}$ is revealed as shown in Fig. 4h. Overall, the $\text{R-CoC}_2\text{O}_4@\text{MXene}$ with unsaturated coordination metal Co sites optimize the Gibbs free energy of HER pathways and electronic structure of the catalyst, so as to promote the HER process.

Electrocatalytic seawater performance of the catalysts

Seawater electrolysis is a promising alternative to conventional freshwater electrolysis due to its abundance and low cost, and it is necessary to evaluate the suitability of using seawater as an electrolyte in the electrolyzer³⁸. Herein, the electrocatalytic HER activity of $\text{R-CoC}_2\text{O}_4@\text{MXene}$ was measured in 1M KOH seawater and natural seawater. $\text{R-CoC}_2\text{O}_4@\text{MXene}$ exhibits the overpotentials of 32 and 163 mV at 10 mA cm^{-1} in 1M KOH seawater and natural seawater (Fig. 5a, b), respectively, which is considerably smaller than Pt/C (64 and 244 mV). Meanwhile, the corresponding Tafel slopes of the $\text{R-CoC}_2\text{O}_4@\text{MXene}$ catalyst are calculated to be around 56 and 120 mV

dec^{-1} , reflecting the better HER kinetics in seawater (Fig. 5c). Moreover, according to the EIS results (Supplementary Fig. 48 and Table 6), a smaller semicircle is observed for $\text{R-CoC}_2\text{O}_4@\text{MXene}$ relative to commercial Pt/C, inferring fast charge transfer in 1M KOH seawater and natural seawater. Remarkably, $\text{R-CoC}_2\text{O}_4@\text{MXene}$ presents robust HER potential stability for 100 h in seawater (Fig. 5d). Meanwhile, compared with the as-prepared $\text{Co(OH)}_2@\text{MXene}$, $\text{R-CoC}_2\text{O}_4@\text{MXene}$ also exhibits the best catalytic performance (Supplementary Fig. 49). After carefully evaluating those state-of-the-art catalysts previously reported, we list $\text{R-CoC}_2\text{O}_4@\text{MXene}$ among the most efficient catalysts for HER in seawater (Fig. 5g and Supplementary Tables 7 and 8). Encouraged by the excellent HER performance of $\text{R-CoC}_2\text{O}_4@\text{MXene}$ hybrids in seawater, an electrolytic cell was assembled to evaluate its potential for overall electrolysis (Fig. 5e). The $\text{R-CoC}_2\text{O}_4@\text{MXene}$ can drive the overall seawater splitting with a cell voltage of 1.47 V (1.0 M KOH), 1.52 V (alkaline seawater), and 1.68 V (natural seawater) at 10 mA cm^{-2} , even outperforming the commercial Pt/C|| RuO_2 (Fig. 5f and Supplementary Fig. 50). $\text{R-CoC}_2\text{O}_4@\text{MXene}$ still exhibits outstanding durability after 30 h of continuous water electrolysis at a current density of 10 mA cm^{-2} (Supplementary Fig. 51). Moreover, the water splitting performance of $\text{R-CoC}_2\text{O}_4@\text{MXene}$ is superior to $\text{Co(OH)}_2@\text{MXene}$ (Supplementary Fig. 52). The faraday efficiency (FE) was assessed by comparing the volumes of produced O_2 and H_2 during

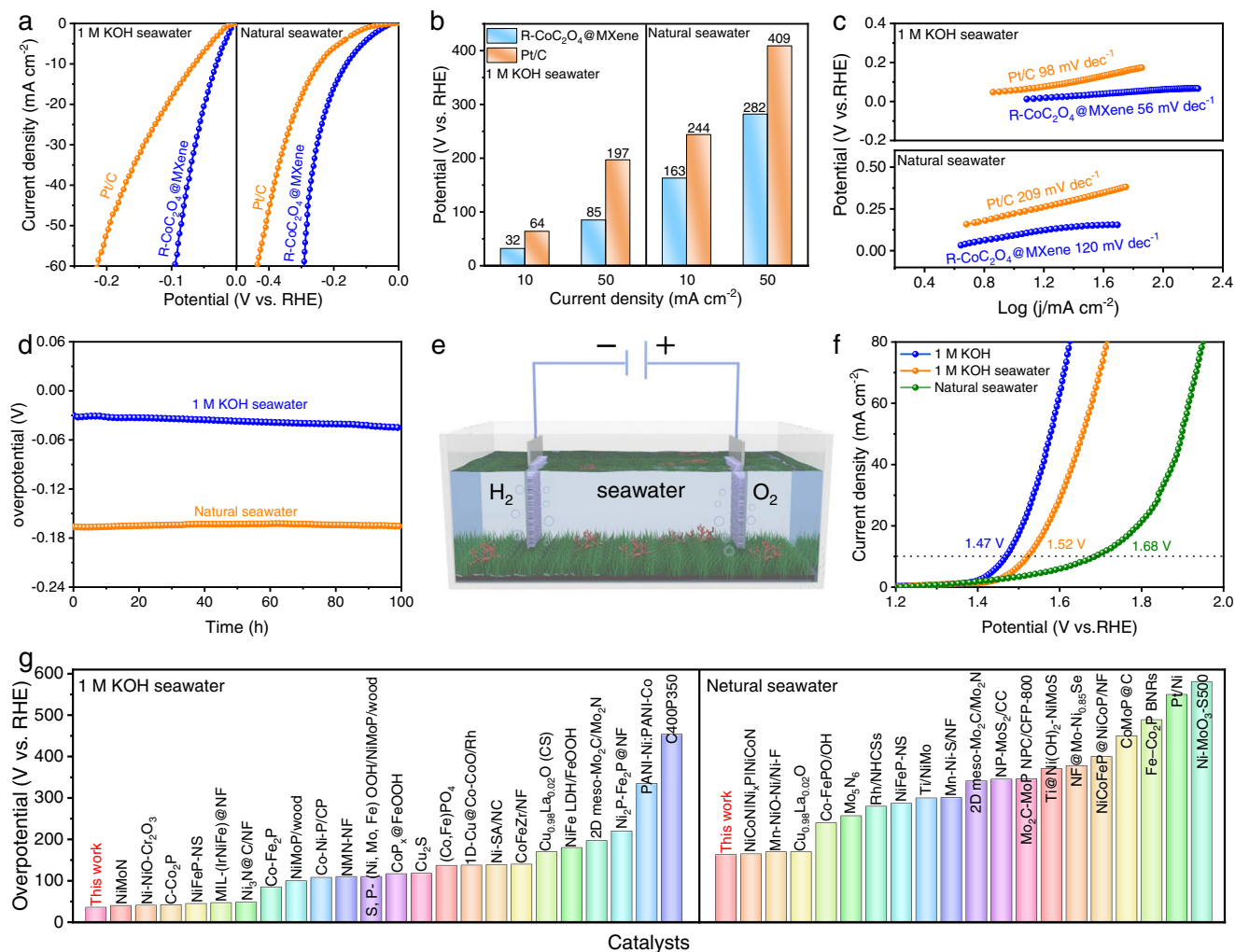


Fig. 5 | Electrochemical seawater performance of the catalysts. a the HER polarization curves, **(b)** overpotential comparison, and **(c)** Tafel slopes of R-Co₂O₄@MXene and commercial Pt/C catalysts recorded in 1 M KOH seawater and natural seawater. **d** Chronopotentiometry curve of R-Co₂O₄@MXene in 1 M

KOH seawater and natural seawater. **e** Schematic illustration of the electrolyze. **f** Polarization curve of the R-Co₂O₄@MXene || R-Co₂O₄@MXene toward overall water splitting in different electrolytes. **g** Comparison of HER overpotential (10 mA cm⁻²) in 1 M KOH seawater and natural seawater.

the experiment process. The amount of evolved O₂ and H₂ matches well with the theoretical value in Supplementary Fig. 53, representing FE close to 100%. These results demonstrate that the R-Co₂O₄@MXene catalyst has fully developed electrochemical performance, which makes it outstanding catalytic activity and stability in seawater electrolytes.

Discussion

In summary, we have delicately designed a novel Co₂O₄@MXene tubular catalyst with rapid complete reconfiguration properties to enhance HER performance. High electronic accessibility and abundant electrolyte diffusion channels induced the spontaneous and instantaneous reconfiguration of Co₂O₄@MXene to form Co(OH)₂@MXene. Rapid reconfiguration can expose plenty of Co sites, thereby resulting in the creation of usable charge transfer orbitals and facilitating the electron transfer process. In-situ characterizations and DFT calculations reveal that the obtained Co(OH)₂@MXene after reconfiguration behave as the real active species, which can tune the electronic structure and optimize the energy barriers of water dissociation and H⁺ intermediates, enhancing the intrinsic activity toward OER. As a result, the reconfigured Co₂O₄@MXene electrocatalyst exhibits brilliant HER performance, which can acquire 10 and 1000 mA cm⁻² at a low overpotential of 28 and 216 mV in alkaline conditions. More

importantly, the HER activity of R-Co₂O₄@MXene is stable in alkaline seawater and natural seawater, which is superior to commercial Pt/C. Our research provides an in-depth understanding into the in-situ reconfiguration of electrocatalysts during HER and facilitates the rational design and controllable synthesis of high-performance catalysts for sustainable hydrogen generation.

Methods

Materials

All the chemicals were used without further purification. Cobalt nitrate hexahydrate (Co(NO₃)₂·6H₂O), oxalic acid dihydrate (H₂C₂O₄·2H₂O), potassium hydroxide (KOH), Ti₃AlC₂ powders (200 mesh), lithium fluoride (LiF), hydrochloric acid (HCl), hexamethylenetetramine (HMT), and platinum on graphitized carbon (Pt/C, 20 wt%) were purchased from Macklin.

Preparation of MXene nanosheets

1 g of Ti₃AlC₂ powders were slowly added to the mixed solution of 2 g of LiF and 30 ml of HCl and magnetically stirred in an oil bath at 45 °C for 36 h to selective removing of Al layers. Subsequently, the acidic mixed solution containing MXene was washed with distilled water several times by centrifugation (2264 xg) until the supernatant reached neutral pH (≥6). The collected precipitate was vacuum dried

to obtain bulk MXene powder. Finally, 0.2 g of MXene powder was dispersed in 300 ml of distilled water and sonicated under Ar atmosphere for 5 h, and then the supernatant was collected by centrifugation.

Preparation of CoC₂O₄@MXene and CoC₂O₄

To prepare CoC₂O₄@MXene, 0.20 g of H₂C₂O₄·2H₂O was dissolved in 20 mL of deionized water to obtain solution A, and then 0.46 g of Co(NO₃)₂·6H₂O was dissolved in a mixed solution of 20 mL of MXene and 10 mL of deionized water to obtain solution B. Subsequently, the solution B was slowly added dropwise into solution A and stirred magnetically for 6 h at room temperature. Finally, the dispersion was collected by centrifugation at 7155 xg for 5 min and washed several times with deionized water, followed by freeze-drying for 12 h. For comparison, we performed control experiments with different (0, 10, 20, and 30 ml) MXene solution under other conditions unchanged, and the products can be labeled as CoC₂O₄, CoC₂O₄@MXene-10, CoC₂O₄@MXene-20 and CoC₂O₄@MXene-30, respectively.

Preparation of Co(OH)₂@MXene and Co(OH)₂

0.36 g of Co(NO₃)₂·6H₂O and 1.68 g of HMT were dissolved in a mixed solution of 150 mL of deionized water and 50 mL of ethanol. Then, 20 mL of MXene solution was added. Subsequently, the reaction solution was heated to about 90 °C for 1 h under magnetic stirring. Finally, the dispersion was collected by centrifugation at 7000 rpm for 5 min and washed several times with deionized water and ethanol, then vacuum dried for 10 h. MXene was not added during the preparation of Co(OH)₂.

Characterizations

The structure and morphology were observed using scanning electron microscopy (SEM, Regulus 8100) and high-resolution transmission electron microscopy (HRTEM, FEI Tecnai G2 F20). The in-situ Raman spectra were collected by RENISHAW at an excitation wavelength of 633 nm. X-ray diffraction (XRD) data obtained from Bruker D8 Advance equipment was used to analyze the crystal structure. X-ray photoelectron spectrometer (XPS) with Al K α X-rays was performed to study the surface composition of the samples. Bruker ENX-500 device was used to measure electron paramagnetic resonance (EPR) data. The Brunauer-Emmett-Teller (BET) surface area was determined using the instrument V-Sorb 2008P. X-ray absorption fine structure spectra were measured under room temperature using the transmission mode of the XAFCA beamline in the Singapore Synchrotron Light Source. Extended X-ray absorption fine structure data were interpreted utilizing WINXAS 3.1 code, where it was normalized and then transformed to momentum space (k) from the initial energy space. The chemical states of the materials were studied by X-ray photoelectron spectroscopy (Thermo ESCALAB 250). The water contact angle was measured using a contact angle analyzer (DO4010 Easy drop, KRUSS), dropping 10 μ L of water droplets from a height of 2.8 cm. The contact angle was recorded when the elapsed time after the water drop reached 1 min.

Electrochemical measurement

Electrocatalytic activity tests were performed in a three-electrode system using an electrochemical workstation (Autolab Instrument). Graphite rod and a KCl-saturated Ag/AgCl electrode were used as the counter electrode (CE) and reference electrode (RE), respectively. The prepared catalyst, Super P, and binder (PVDF) were mixed in a mass ratio of 7:2:1 to acquire a catalyst slurry. The slurry was coated on 1 \times 1 cm² of nickel foam as the working electrode (loaded mass was around 1.5 mg cm⁻²). The potentials were normalized to the reversible hydrogen electrode (RHE) by the Nernst equation ($E_{\text{RHE}} = E_{\text{Ag/AgCl}} + 0.198 + 0.0591 \times \text{pH}$)⁵⁰. Polarization curves were measured by linear sweep voltammetry (LSV) at a scan rate of 5 mV s⁻¹ and compensated using iR. Cyclic

voltammograms (CV) were recorded at increasing scan rates (20–100 mV s⁻¹) within the Faradaic potential window (0.42–0.52 V vs. RHE) to obtain electrochemical surface area (ECSA). Electrochemical impedance spectroscopy (EIS) was performed in the frequency range of 0.1–105 Hz with an amplitude of 5 mV.

Calculation methods

We have employed the first principles to perform all density functional theory (DFT) calculations within the generalized gradient approximation (GGA) and utilize the Perdew–Burke–Ernzerhof (PBE) formulation⁵¹. We have chosen projected enhanced wave (PAW) potentials to describe the ionic cores and take valence electrons into account using a plane-wave basis set with a kinetic energy cutoff of 450 eV. Partial occupancies of the Kohn-Sham orbitals were allowed by applying the Gaussian smearing method and a width of 0.05 eV. Convergence values for energy change and geometry optimization were set as 0.03 eV \AA^{-1} and 10⁻⁴ eV, respectively. Dispersive interactions were described by Grimme's DFT-D3 method. The Brillouin zone was sampled using a 1 \times 1 \times 1 uniform Monkhorst-Pack k grid. Finally, the adsorption energies (E_{ads}) were calculated as $E_{\text{ads}} = E_{\text{ad/sub}} - E_{\text{ad}} - E_{\text{sub}}$, where $E_{\text{ad/sub}}$, E_{ad} , and E_{sub} are the total energies of the optimized adsorbate/substrate system, the adsorbate in the structure, and the clean substrate, respectively. The free energy was calculated using the equation:

$$G = E + \text{APE} - \text{TS} \quad (1)$$

where G, E, ZPE, and TS are the free energy, total energy from DFT calculations, zero-point energy, and entropic contributions, respectively.

Data availability

The data that support the findings of this study are available from the corresponding authors upon reasonable request. Source data are provided with this paper.

References

- Dinh, C.-T. et al. Multi-site electrocatalysts for hydrogen evolution in neutral media by destabilization of water molecules. *Nat. Energy* **4**, 107–114 (2019).
- Podjaski, F. et al. Rational strain engineering in delafossite oxides for highly efficient hydrogen evolution catalysis in acidic media. *Nat. Catal.* **3**, 55–63 (2020).
- Jin, H. et al. Stable and highly efficient hydrogen evolution from seawater enabled by an unsaturated nickel surface nitride. *Adv. Mater.* **33**, 2007508 (2021).
- Deng, L. et al. Electronic modulation caused by interfacial Ni–O–M (M= Ru, Ir, Pd) bonding for accelerating hydrogen evolution kinetics. *Angew. Chem. Int. Ed.* **60**, 22276–22282 (2021).
- Liu, M. et al. Interfacial electronic structure engineering on molybdenum sulfide for robust dual-pH hydrogen evolution. *Nat. Commun.* **12**, 5260 (2021).
- Zhao, G., Li, P., Cheng, N., Dou, S. X. & Sun, W. An Ir/Ni(OH)₂ heterostructured electrocatalyst for the oxygen evolution reaction: breaking the scaling relation, stabilizing iridium(V), and beyond. *Adv. Mater.* **32**, 2000872 (2020).
- Zheng, X. et al. Non-carbon-supported single-atom site catalysts for electrocatalysis. *Energy Environ. Sci.* **14**, 2809–2858 (2021).
- Wu, X. et al. Solvent-free microwave synthesis of ultra-small Ru–Mo₂C@CNT with strong metal-support interaction for industrial hydrogen evolution. *Nat. Commun.* **12**, 4018 (2021).
- Guo, X. et al. Phosphated IrMo bimetallic cluster for efficient hydrogen evolution reaction. *eScience* **2**, 304–310 (2022).
- Bai, Y. et al. Near-equilibrium growth of chemically stable covalent organic framework/graphene oxide hybrid materials for the

- hydrogen evolution reaction. *Angew. Chem. Int. Ed.* **61**, e202113067 (2022).
- Wu, Z.-P. et al. Manipulating the local coordination and electronic structures for efficient electrocatalytic oxygen evolution. *Adv. Mater.* **33**, 2103004 (2021).
 - Zheng, X. et al. Multifunctional active-center-transferable platinum/lithium cobalt oxide heterostructured electrocatalysts towards superior water splitting. *Angew. Chem. Int. Ed.* **59**, 14533–14540 (2020).
 - Huang, H. et al. Clusters induced electron redistribution to tune oxygen reduction activity of transition metal single-atom for metal–air batteries. *Angew. Chem. Int. Ed.* **61**, e202116068 (2022).
 - Song, J. et al. Sub-2 nm thiophosphate nanosheets with heteroatom doping for enhanced oxygen electrocatalysis. *Adv. Funct. Mater.* **31**, 2100618 (2021).
 - Dai, T. et al. Uncovering the promotion of CeO₂/CoS_{1.97} heterostructure with specific spatial architectures on oxygen evolution reaction. *Adv. Mater.* **33**, 2102593 (2021).
 - Liu, X. et al. Reconstruction-determined alkaline water electrolysis at industrial temperatures. *Adv. Mater.* **32**, 2001136 (2020).
 - Du, W., Shi, Y., Zhou, W., Yu, Y. & Zhang, B. Unveiling the in situ dissolution and polymerization of Mo in Ni₄Mo alloy for promoting the hydrogen evolution reaction. *Angew. Chem. Int. Ed.* **60**, 7051–7055 (2021).
 - Bai, J. et al. Molybdenum-promoted surface reconstruction in polymorphic cobalt for initiating rapid oxygen evolution. *Adv. Energy Mater.* **12**, 2103247 (2022).
 - Sun, Y. et al. Nitrogen-doped cobalt diselenide with cubic phase maintained for enhanced alkaline hydrogen evolution. *Angew. Chem. Int. Ed.* **60**, 21575–21582 (2021).
 - Wang, J. et al. Redirecting dynamic surface restructuring of a layered transition metal oxide catalyst for superior water oxidation. *Nat. Catal.* **4**, 212–222 (2021).
 - Sun, Y. et al. A-site management prompts the dynamic reconstructed active phase of perovskite oxide OER catalysts. *Adv. Energy Mater.* **11**, 2003755 (2021).
 - He, L. et al. Molybdenum carbide-oxide heterostructures: in situ surface reconfiguration toward efficient electrocatalytic hydrogen evolution. *Angew. Chem. Int. Ed.* **59**, 3544–3548 (2020).
 - Li, X. et al. Adaptive bifunctional electrocatalyst of amorphous CoFe oxide @ 2D black phosphorus for overall water splitting. *Angew. Chem. Int. Ed.* **59**, 21106–21113 (2020).
 - Yuan, L. et al. Modulation of Volmer step for efficient alkaline water splitting implemented by titanium oxide promoting surface reconstruction of cobalt carbonate hydroxide. *Nano Energy* **82**, 105732 (2021).
 - Solomon, G. et al. NiMoO₄@Co₃O₄ core-shell nanorods: in situ catalyst reconstruction toward high efficiency oxygen evolution reaction. *Adv. Energy Mater.* **11**, 2101324 (2021).
 - Duan, Y. et al. Anodic oxidation enabled cation leaching for promoting surface reconstruction in water oxidation. *Angew. Chem. Int. Ed.* **60**, 7418–7425 (2021).
 - Xiao, Z. et al. Operando identification of the dynamic behavior of oxygen vacancy-rich Co₃O₄ for oxygen evolution reaction. *J. Am. Chem. Soc.* **142**, 12087–12095 (2020).
 - Wu, T. et al. Iron-facilitated dynamic active-site generation on spinel CoAl₂O₄ with self-termination of surface reconstruction for water oxidation. *Nat. Catal.* **2**, 763–772 (2019).
 - Liu, X. et al. Complete reconstruction of hydrate pre-catalysts for ultrastable water electrolysis in industrial-concentration alkali media. *Cell Rep. Phys. Sci.* **1**, 100241 (2020).
 - Ji, P. et al. Ultra-fast and in-depth reconstruction of transition metal fluorides in electrocatalytic hydrogen evolution processes. *Adv. Sci.* **9**, 2103567 (2022).
 - Liu, X. et al. Ligand and anion Co-leaching induced complete reconstruction of polyoxomolybdate-organic complex oxygen-evolving pre-catalysts. *Adv. Funct. Mater.* **31**, 2101792 (2021).
 - Li, L. et al. Interfacial electronic coupling of ultrathin transition-metal hydroxide nanosheets with layered MXenes as a new prototype for platinum-like hydrogen evolution. *Energy Environ. Sci.* **14**, 6419–6427 (2021).
 - Wu, X. et al. Engineering multifunctional collaborative catalytic interface enabling efficient hydrogen evolution in all pH range and seawater. *Adv. Energy Mater.* **9**, 1901333 (2019).
 - Yu, M. et al. A hierarchically porous and hydrophilic 3D nickel-iron/MXene electrode for accelerating oxygen and hydrogen evolution at high current densities. *Nano Energy* **63**, 103880 (2019).
 - Zhang, C. et al. High-throughput production of cheap mineral-based two-dimensional electrocatalysts for high-current-density hydrogen evolution. *Nat. Commun.* **11**, 3724 (2020).
 - Ji, X. et al. Graphene/MoS₂/FeCoNi(OH)_x and graphene/MoS₂/FeCoNiP_x multilayer-stacked vertical nanosheets on carbon fibers for highly efficient overall water splitting. *Nat. Commun.* **12**, 1380 (2021).
 - Jiang, S. et al. Promoting formation of oxygen vacancies in two-dimensional cobalt-doped ceria nanosheets for efficient hydrogen evolution. *J. Am. Chem. Soc.* **142**, 6461–6466 (2020).
 - Yu, L. et al. Non-noble metal-nitride based electrocatalysts for high-performance alkaline seawater electrolysis. *Nat. Commun.* **10**, 5106 (2019).
 - Li, S., Zhao, Z., Ma, T., Pachfule, P. & Thomas, A. Superstructures of organic-polyoxometalate Co-crystals as precursors for hydrogen evolution electrocatalysts. *Angew. Chem. Int. Ed.* **61**, e202112298 (2022).
 - Du, C.-F. et al. Self-assemble and in situ formation of Ni_{1-x}Fe_xPS₃ nanomosaic-decorated MXene hybrids for overall water splitting. *Adv. Energy Mater.* **8**, 1801127 (2018).
 - Chen, C. et al. Epitaxially grown heterostructured SrMn₃O_{6-x}-SrMnO₃ with high-valence Mn^{3+/4+} for improved oxygen reduction catalysis. *Angew. Chem. Int. Ed.* **60**, 22043–22050 (2021).
 - Ramalingam, V. et al. Heteroatom-mediated interactions between ruthenium single atoms and an MXene support for efficient hydrogen evolution. *Adv. Mater.* **31**, 1903841 (2019).
 - Ye, S.-H., Shi, Z.-X., Feng, J.-X., Tong, Y.-X. & Li, G.-R. Activating CoOOH porous nanosheet arrays by partial iron substitution for efficient oxygen evolution reaction. *Angew. Chem. Int. Ed.* **57**, 2672–2676 (2018).
 - Zhao, Y. et al. Dynamics and control of active sites in hierarchically nanostructured cobalt phosphide/chalcogenide-based electrocatalysts for water splitting. *Energy Environ. Sci.* **15**, 727–739 (2022).
 - Wang, T., Cao, X. & Jiao, L. Ni₂P/NiMoP heterostructure as a bifunctional electrocatalyst for energy-saving hydrogen production. *eScience* **1**, 69–74 (2021).
 - Luo, Y. et al. Stabilized hydroxide-mediated nickel-based electrocatalysts for high-current-density hydrogen evolution in alkaline media. *Energy Environ. Sci.* **14**, 4610–4619 (2021).
 - Zhou, K. L. et al. Platinum single-atom catalyst coupled with transition metal/metal oxide heterostructure for accelerating alkaline hydrogen evolution reaction. *Nat. Commun.* **12**, 3783 (2021).
 - Dai, J. et al. Single-phase perovskite oxide with super-exchange induced atomic-scale synergistic active centers enables ultrafast hydrogen evolution. *Nat. Commun.* **11**, 5657 (2020).
 - Yang, Y. et al. O-coordinated W-Mo dual-atom catalyst for pH-universal electrocatalytic hydrogen evolution. *Sci. Adv.* **6**, eaba6586 (2020).
 - Li, X. et al. Sequential electrodeposition of bifunctional catalytically active structures in MoO₃/Ni-NiO composite electrocatalysts for selective hydrogen and oxygen evolution. *Adv. Mater.* **32**, 2003414 (2020).

51. Perdew, J. P., Burke, K. & Ernzerhof, M. Generalized gradient approximation made simple. *Phys. Rev. Lett.* **77**, 3865–3868 (1996).

Acknowledgements

This work was supported by the National Natural Science Foundation of China (51871119, S.-P., 22075141, S.-P., and 22101132, F.-H.), Scientific and Technological Innovation Special Fund for Carbon Peak and Carbon Neutrality of Jiangsu Province (BK20220039), Jiangsu Provincial Funds for Natural Science Foundation (BK20210311, S.-P.), China Postdoctoral Science Foundation (2021M691561, F.-H. and 2021T140319, F.-H.), Post-graduate Research & Practice Innovation Program of NUAA (xcxjh20210607, L.-W.), Scientific and Technological Innovation Special Fund for Carbon Peak and Carbon Neutrality of Jiangsu Province (BK20220039, S.-P.), and Jiangsu Postdoctoral Research Fund (2021K547C, F.-H.).

Author contributions

S.P. and L.W. conceived the project and designed the experiments. L.W. performed the synthesis and characterization of catalysts and the electrocatalytic measurements. Y.H., L.D., L.W., and S.Z. was involved in the structural and electrochemical analysis. L.W. wrote the paper. S.P., F.H., and L.L. contributed to revising the manuscript. All authors discussed the results and commented on the paper.

Competing interests

The authors declare no competing interests.

Additional information

Supplementary information The online version contains supplementary material available at <https://doi.org/10.1038/s41467-022-33590-5>.

Correspondence and requests for materials should be addressed to Shengjie Peng.

Peer review information *Nature Communications* thanks Kuo-Wei Huang and the other, anonymous, reviewers for their contribution to the peer review of this work. Peer reviewer reports are available.

Reprints and permission information is available at <http://www.nature.com/reprints>

Publisher's note Springer Nature remains neutral with regard to jurisdictional claims in published maps and institutional affiliations.

Open Access This article is licensed under a Creative Commons Attribution 4.0 International License, which permits use, sharing, adaptation, distribution and reproduction in any medium or format, as long as you give appropriate credit to the original author(s) and the source, provide a link to the Creative Commons license, and indicate if changes were made. The images or other third party material in this article are included in the article's Creative Commons license, unless indicated otherwise in a credit line to the material. If material is not included in the article's Creative Commons license and your intended use is not permitted by statutory regulation or exceeds the permitted use, you will need to obtain permission directly from the copyright holder. To view a copy of this license, visit <http://creativecommons.org/licenses/by/4.0/>.

© The Author(s) 2022